Li et al. *Microsystems & Nanoengineering* (2026)12:35
https://doi.org/10.1038/s41378-026-01167-7

Microsystems & Nanoengineering
www.nature.com/micronano

ARTICLE Open Access

Large-scale optical trapping using a gradient-thickness protected microbottle resonator

Yuxiang Li[1,2,3], Haotian Wang[4], Zhihe Guo[1], Xuyang Zhao[1], Yi Zhou[1], Qi Wang[1], Man Luo[1], Hong Cai[2,3], Lip Ket Chin[2,3]✉, Ai-Qun Liu[2,3]✉ and Xiang Wu[1]✉

Abstract

Despite its huge potential, such as in biomedical research for bioparticle sorting and sensing, near-field optical trapping suffers from limited trapping efficiency due to the weak evanescent field accompanied by shallow penetration depth (~100 nm). Moreover, such optical trapping approaches are susceptible to perturbations from trapped particles, making them less robust and impractical. Here, we demonstrate, for the first time, a thin-walled hollow microbottle resonator with gradient-wall thickness to realize large-scale and robust optical trapping based on mode field strength antinodes, instead of the evanescent field. The microbottle resonator combined with off-equatorial fiber taper coupling collaboratively enables the excitation of axial high-order Whispering Gallery Modes (WGMs). In addition, the unique feature of the gradient-wall thickness design mitigates the adverse impact of the perturbation from trapped particles on mode field distributions, making the gradient-thickness protected (GTP) microbottle resonator more robust and stable. This enables large-scale optical trapping over an axial span exceeding 195 μm, with a threshold power of 0.198 mW for 500-nm-radius polystyrene particles. The GTP WGM microbottle resonator also achieves tunable localized optical trapping. This work demonstrates a scalable optical manipulation framework for applications in single-particle analysis, bioparticle manipulation, and label-free sensing.

Introduction

Near-field optical trapping has advanced tremendously with the synergic integration of photonics and fluidics, enabling precise manipulation and sorting of particles down to the nano-sized regime beyond the traditional diffraction limit[1–3] in conventional optical tweezers. It has been studied intensively across various scientific fields, including biomedical research[4–8], chemistry[9], and even atomic physics[10–12]. For instance, various nanowaveguide or metasurface designs were demonstrated for trapping, sorting and detecting bacteria, viruses, or nucleic acid[4,6,7].

Optofluidic whispering-gallery-mode (WGM) microresonators, such as microrings[13–17], microspheres[18–20], microbubbles[9,21], microdisks[22], and droplets[23], have emerged as versatile platforms for particle trapping, sorting and sensing. Their high quality (Q) factors and subwavelength-scale mode volumes significantly enhance intracavity field intensities, facilitating strong light–matter interactions. However, conventional WGM-based particle trapping primarily relies on evanescent fields, which are inherently weak and typically confined to depths of ~100 nm near the particle-interacting interface. This shallow penetration limits trapping efficiency and restricts particle manipulation in close proximity to the resonator surface. Furthermore, in typical quasi-droplet WGM resonators, the optical mode is concentrated in the liquid core near the inner surface of the resonator, rendering it susceptible to perturbations from trapped particles. Such disruptions degrade the Q factor and reduce the intracavity field intensity, undermining the optical forces needed for robust nanoparticle trapping. As a result, conventional WGMs struggle to generate sufficient force for trapping smaller nanoparticles, and their effective trapping region is constrained, posing challenges for

Correspondence: Lip Ket Chin (lipket.chin@polyu.edu.hk) or Ai-Qun Liu (aiqun.liu@polyu.edu.hk) or Xiang Wu (wuxiang@fudan.edu.cn)
[1]College of Future Information Technology, State Key Laboratory of Photovoltaic Science and Technology, Fudan University, Shanghai, China
[2]Research Institute for Quantum Technology (RIQT), The Hong Kong Polytechnic University, Hong Kong SAR, China
Full list of author information is available at the end of the article
These authors contributed equally: Yuxiang Li, Haotian Wang

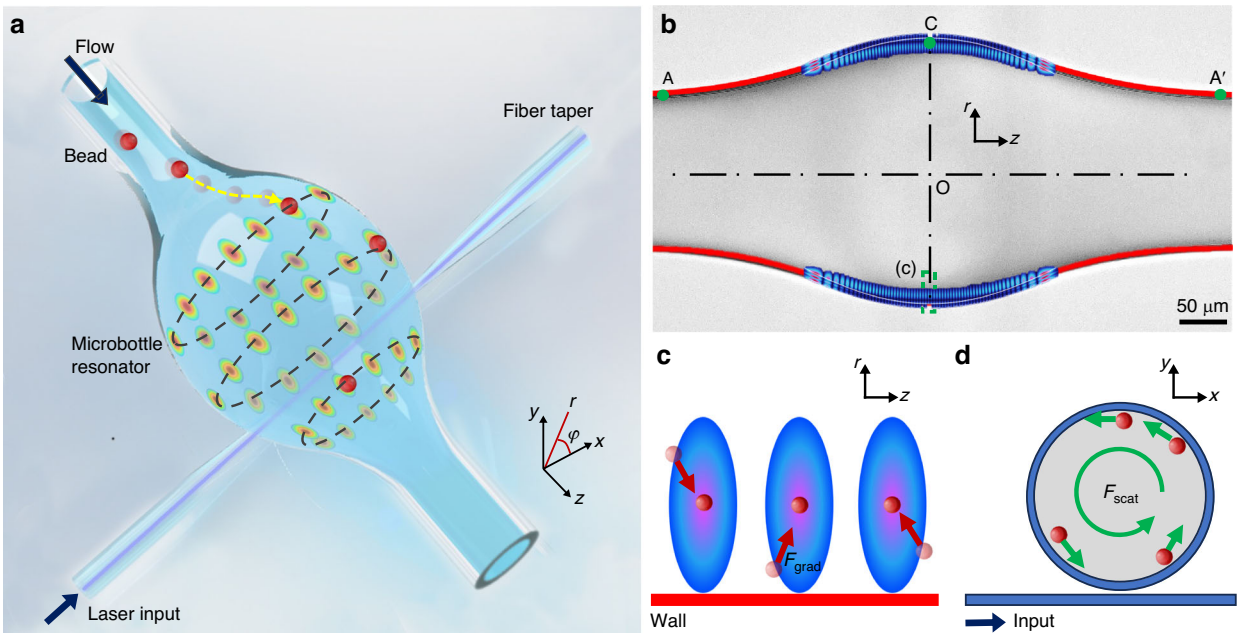

Fig. 1 Gradient-thickness-protected WGM microbottle resonator for large-scale particle trapping. a Schematic of particle trapping in the microbottle WGM resonator. **b** Microscope image of the microbottle, overlaid with simulated optical hotspots near the inner wall. **c** Zoomed-in *rz*-view of the optical hotspots at equatorial center, showing the action of the optical gradient force. **d** *xy*-view showing the action of the optical scattering force

applications requiring dense, high-efficiency nanoparticle manipulation.

To overcome the limitations of conventional WGM resonators, we present a thin-walled hollow microbottle resonator that enables direct interaction between the WGM field strength antinodes and suspended particles, achieving deeper penetration and stronger light–matter interaction without relying solely on weak evanescent fields. The gently curved geometry of the microbottle, combined with off-equatorial fiber taper coupling, supports the excitation of high-order axial modes[24]. A key factor enabling this mode selectivity is that the coupling strength for a specific WGM is proportional to the spatial overlap integral between the mode fields of the resonator and the fiber taper[25]. This mechanism facilitates large-scale particle trapping along multiple orbits across an extended axial range with only milliwatt-level optical power. Additionally, the resonator features a gradient wall thickness that confines the peak optical intensity within the structure, isolating it from disturbances caused by trapped particles and thereby enhancing trapping stability. The device further enables localized three-dimensional particle confinement by leveraging standing waves formed by counter-propagating WGMs. Phase shifts introduced via a piezoelectric fiber stretcher allow dynamic adjustment and repositioning of the particle traps. The hollow architecture of the microbottle resonator facilitates seamless integration with microfluidic channels, yielding a gradient-thickness-protected (GTP) WGM platform optimized for efficient particle manipulation. Compared to previously reported near-field trapping techniques, the GTP microbottle resonator offers a simplified configuration, improved trapping robustness, and scalable large-area particle confinement. These advantages position the device as a promising tool for enhancing the efficiency of bioparticle sorting and enabling practical, localized optical manipulation in biological and chemical sensing and analysis.

Theoretical Analysis

Gradient-Thickness-Protected WGM Resonator

Optical trapping in resonant systems, such as the WGM microbottle resonator, exploits two fundamental forces, *i.e.*, the optical gradient force and the optical scattering force. The gradient force arises from the spatial inhomogeneity of the light intensity, creating a potential well that attracts particles to the positions of electric intensity maxima, thereby achieving stable confinement. In contrast, the scattering force stems from momentum transfer as photons interact with the particle, driving propulsion along the beam's direction via radiation pressure. These forces, amplified by high-Q resonators, enable precise manipulation.

Figure 1 illustrates the GTP WGM microbottle resonator, formed by a hollow optofluidic microbottle with a tapered wall profile: the equatorial center (**C**) has a wall

thickness of 1μm, while the axial ends (**A** and **A'**) measure 5 μm. To excite WGMs, a fiber taper is used to evanescently couple laser light into the resonator (Fig. 1a). In the resonator, the optical field propagates as a traveling wave along the azimuthal direction (*i.e.*, φ-axis). Simultaneously, the excited WGM forms an array of eigenmode field strength antinodes (optical hotspots) along the axial (*i.e.*, z-axis) and radial (*i.e.*, r-axis) directions near the inner wall (Fig. 1b). These optical hotspots enable large-scale particle confinement whereby the optical gradient force draws particles toward and aligns them along the centers of the hotspots (Fig. 1c), and the optical scattering force induces rotational motion near the inner wall (Fig. 1d). The direction of the resulting circular particle trajectories corresponds to and aligns with the laser input direction.

The gradient-thickness thinned-wall design of the microbottle resonator offers two key performance advantages over conventional WGMs. First, near the equatorial region, the thinned wall enables the coupled optical field to leak almost entirely into the liquid core across a hotspot region spanning several micrometers (Fig. 1b). This results in a significantly larger optical force and trapping region compared to the shallow, 100-nm-scale evanescent waves in traditional WGMs, thereby reducing the required optical power and enhancing particle manipulation efficiency. Second, the peak optical field at both ends (**P** and **P'**) remains confined within the fused glass capillaries (Fig. 2a), shielding it from interference by trapped particles. In contrast, conventional WGMs expose the peak optical field at both ends, making them vulnerable to perturbations of trapped particles that diminish intracavity field intensity and weaken optical trapping stability. The GTP WGM microbottle resonator mitigates this issue by localizing the peak optical field within the resonator, which is further explored in the next section.

E-field distribution Analysis

To highlight the superiority of the GTP WGM microbottle resonator as compared to a uniform thickness one, a two-dimensional axisymmetric model based on the finite element method (FEM) was employed in COMSOL Multiphysics software to simulate the mode field distributions in both cases. WGMs in a microbottle resonator are characterized by three quantum numbers (m, p, q), denoting the azimuthal, radial, and axial orders, respectively. All simulations were conducted with a fixed azimuthal order of $m = 875$ to ensure a resonant wavelength near 950 nm. Figure 2a, b shows the electric field (E-field) distribution in the GTP and uniform thickness WGM microbottle resonators, with radial and axial mode orders (p, q) of (3, 61) and (3, 53), respectively. The confinement of WGMs relies on total internal reflection at the resonator's outer surface. A reduction in the local wall thickness thus causes higher-order radial components of the mode to leak from the silica wall into the liquid core. Due to the overall thin wall, both configurations exhibit most E-field antinodes localized within the liquid core (several μm from the inner surface).

Furthermore, the excitation of high-order axial modes leads to an extended field distribution along the microbottle axis. The axial E-field profile resembles high-order Hermite functions[26], naturally resulting in two intensity maxima at the axial ends. The GTP WGM microbottle resonator strategically leverages its axial wall-thickness gradient to manage these inherent field properties: the thicker walls at both axial ends (**P and P'**) confine the peak E-field within the silica wall (Fig. 2c) to maintain a high-Q resonance, while the thinner wall at the equatorial center (**C**) allows a portion of the mode to leak into the liquid core (Fig. S1), enabling efficient particle trapping. In contrast, in the uniform thickness WGM microbottle resonator, almost all E-fields are localized within the liquid core, including the peak E-fields at both ends (Fig. 2d), which will be perturbed significantly when particles are being trapped at the peak E-field position. Furthermore, since silica has much lower absorption for 950-nm infrared light compared to deuterium oxide (D_2O, heavy water), medium used in the experiments, the GTP WGM that confines the peak E-field within the silica wall theoretically has a higher Q factor than the uniform thickness one with peak E-field in the liquid core.

Assuming critical coupling between the fiber taper and the microbottle resonator, the intracavity field enhancement factor (B) is defined as[27]

$$B = \frac{\lambda_0 Q}{4\pi n_{\text{eff}} L} \frac{1}{1 + 4Q^2(\Delta\lambda/\lambda_0)^2} \tag{1}$$

where λ_0 is the resonant wavelength of the microbottle resonator, Q and n_{eff} are the Q factor and effective refractive index of the WGM, respectively. L is the trajectory length that the WGM travels around the microbottle resonator in a single lap. $\Delta\lambda/\lambda_0$ is the relative resonant wavelength shift due to trapped particle perturbation, which is expressed as

$$\Delta\lambda/\lambda_0 = 4\pi\varepsilon_0 R_p^3 \frac{\varepsilon_p - \varepsilon_m}{\varepsilon_p + 2\varepsilon_m} \frac{|E_p|^2}{\int \varepsilon_0 \varepsilon_m |E_c|^2 dV} \tag{2}$$

where ε_0 is the electric constant, ε_p and ε_m are the relative dielectric constants of the trapped particle and liquid medium in the microbottle, respectively. R_p is the radius of the trapped particle, E_p is the electric field intensity at the particle position, and E_c represents the electric field intensity distribution in the microbottle resonator.

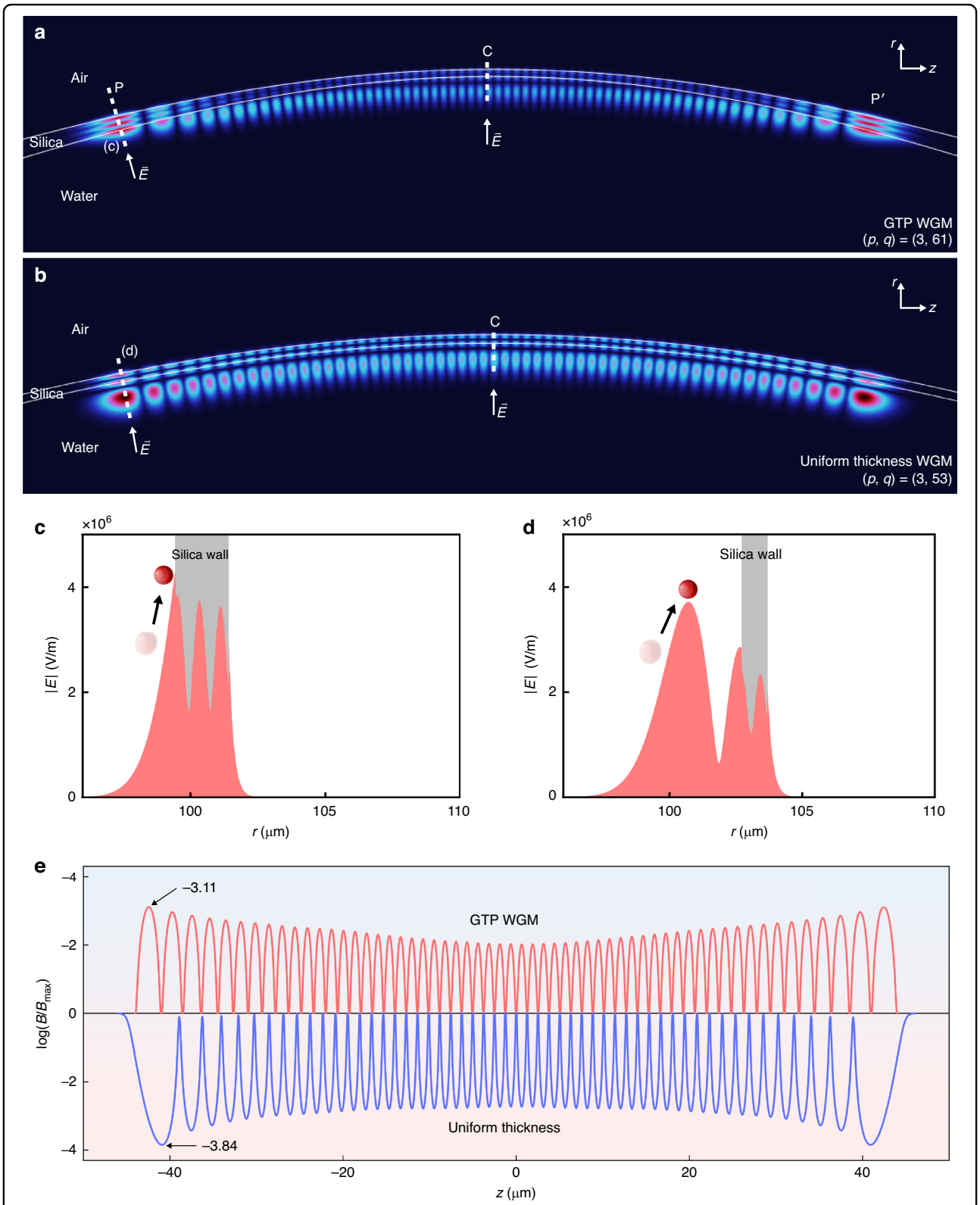

Fig. 2 Electric field distribution analysis. Simulated *E*-field intensity (perpendicular to microbottle surface) in **a** GTP, and **b** uniform thickness WGM microbottle resonators. White solid lines represent inner and outer surface contours of the silica microbottle, respectively. **c**, **d** Respective cross-sectional *E*-field distribution at points highlighted in **a, b**, showing the particle trapping site (red sphere) relative to the silica microbottle wall (gray area). **e** Relative attenuation ratio of *B* induced by a trapped particle at axial position *z* in uniform thickness (blue line) and GTP WGM (red line) microbottle resonator

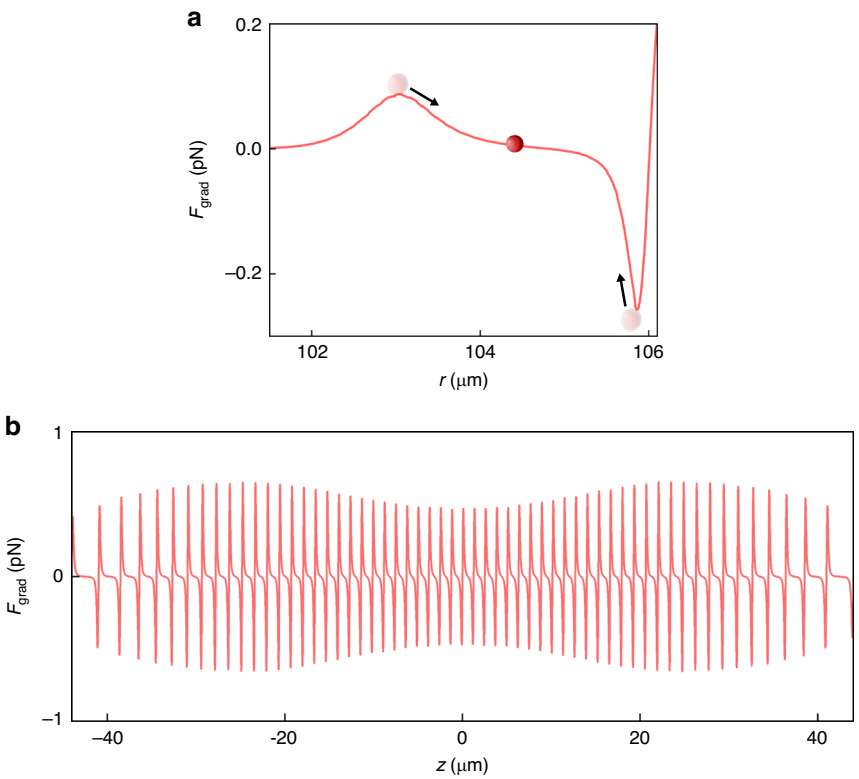

Fig. 3 Simulated optical gradient force exerted on a 500-nm-radius PS particle in the GTP WGM microbottle resonator. a radial (*r*-direction) component of the gradient force. **b** axial (*z*-direction) component of the gradient force

Optical resonators facilitate efficient and effective particle trapping because of the amplified intracavity field intensities (high value of B). However, trapped particles inevitably induce a resonant wavelength shift ($\Delta\lambda$), more significant when the E-field intensity at the particle position (E_p) is large (Eq. (2)). This, in turn, substantially attenuates the intracavity field intensity based on Eq. (1), and affect the particle trapping efficiency significantly. Figure 2e illustrates the relative attenuation ratio of the intracavity field enhancement factor (B) for both microbottle resonators when a 500-nm-radius polystyrene (PS) particle is trapped at different axial positions, presented on a logarithmic scale. Here, the maximum intracavity field enhancement factor $B_{\max}$ is defined as $\lambda_0 Q/4\pi n_{\text{eff}} L$, representing the case without particle perturbation. As shown in Fig. 2e, comparison of the worst-case relative attenuation ratio (B/B_{max}) at the axial position of peak E-field intensity (where particle-induced perturbation is maximal) of the two microbottle resonators ($10^{-3.11}/10^{-3.84}$) reveals that the uniform thickness microbottle resonator exhibits a 5.37-fold higher attenuation than the GTP WGM microbottle resonator. This demonstrates that the GTP WGM microbottle resonator possesses markedly greater tolerance to large-scale particle trapping. The GTP WGM resonator's dual functionality stabilizes the resonant frequency and maintains intracavity field intensities during trapping, thus providing robust and efficient multiple particle manipulation in the optofluidic microbottle resonator.

Optical Force Analysis for Particle Trapping

For a particle trapped by the GTP WGM microbottle resonator, the optical gradient force is defined as[21]

$$F_{grad} = BP\pi\varepsilon_0 \nabla |E_N|^2 R_p^3 \frac{\varepsilon_p - \varepsilon_m}{\varepsilon_p + 2\varepsilon_m} \tag{3}$$

where P is the input power from the fiber taper to the microbottle resonator, and E_N is the normalized electric field of the GTP WGM, *i.e.*, $E_N = N_c E_c$. The normalization coefficient N_c is expressed as

$$N_c^2 = \frac{2\sqrt{\mu_0}}{\sqrt{\varepsilon_0 \varepsilon_m} \iint |E_c|^2 dx \cdot dy} \tag{4}$$

where μ_0 is the magnetic constant. Particle trapping is achieved by the optical gradient forces acting in both radial and axial directions. In the simulation, the light wavelength is set to 952 nm, with a Q factor of 10^7 and an incident power (P) of 1 mW. The calculated $B_{\max}$ is 909

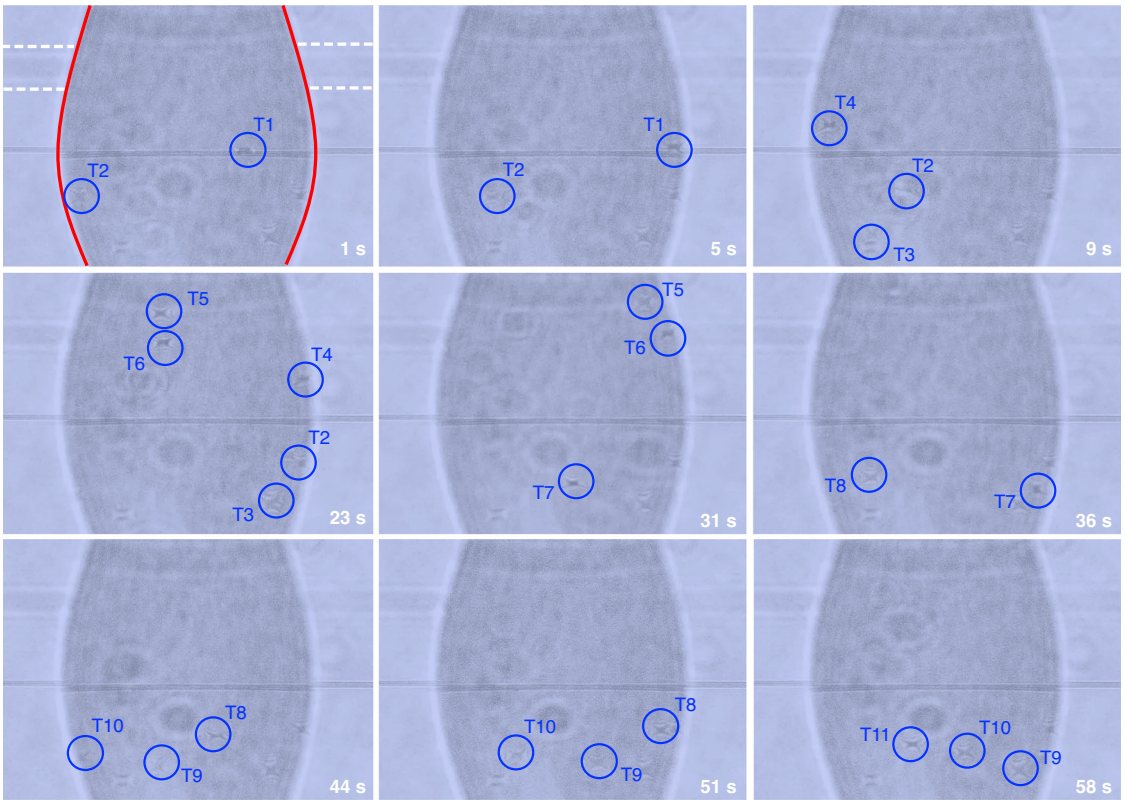

Fig. 4 Representative microscopic images extracted from Supplementary Movie 1, demonstrating large-scale PS particle trapping in the GTP WGM microbottle resonator under an input power of 1.03 mW. Red curves represent the boundary of the microbottle. The fiber taper between the white dashed lines served as the optical coupler for high-order axial WGMs, whereas the central fiber taper (line at the center) remained inactive. Blue circles highlight the trapped particles, which rotate along multiple equatorial trajectories

according to Eq. (1). The optical gradient forces on a 500-nm-radius PS particle along the radial and axial directions are shown in Fig. 3a, b, respectively. In the radial direction (*i.e.*, r-axis), the gradient force on the particle becomes zero at $r \approx 104.8\,\mu m$, indicating that the particle is confined to a position 2 μm away from the microbottle's inner surface. Along the axial direction (*i.e.*, z-axis), the gradient force has zero values at multiple positions (58 hotspots), forming a series of stable trapping orbits that enable large-scale optical trapping. Meanwhile, the propagating GTP WGM exerts an optical scattering force in the azimuthal direction (*i.e.*, φ-axis) on the trapped particles, establishing a dual-action mechanism: the gradient force pushes the particles toward the inner surface and confines them at multiple discrete axial antinodes, while the scattering force propels the particles along circular trajectories via momentum transfer.

Experimental Results And Discussion

Fabrication process and experimental setup

As shown in Fig. S2, the thin-walled hollow optofluidic microbottle resonator was fabricated from glass capillaries (TSP075150, Polymicro Technologies) via a fuse-and-blow technique. A glass capillary was first etched with hydrofluoric acid to thin its walls to 5 μm. One end was then sealed using a fiber fusion splicer via high-voltage discharge. The other end was connected to a syringe via a Teflon tube. Multiple discharges were performed to melt and soften the glass capillary while the syringe was pushed to apply air pressure; the combined action expanded the capillary and formed a slightly bulging microbottle structure. The microbottle has an equatorial wall thickness as thin as 1 μm and an equatorial diameter of 215.72 μm (Fig. 1b). The outer contour of the microbottle can be approximately fitted with a Gaussian line shape as[28]

$$r_{\mathrm{outer}}(z)[\mu m] = 62.55 + 45.31 \cdot e^{-5.64 \times 10^{-5} z^2} \quad (5)$$

where 62.55 μm is the outer radius of the capillary, and 107.86 μm ($r_{\mathrm{outer}}(z=0)$) is the outer equatorial radius of the microbottle. Microscopic measurements confirm that the microbottle structure exhibits a wall thickness of 5 μm at its capillary portion and 1 μm at the equatorial region. Since the volume of glass remains the same during the transformation from capillary to microbottle, the inner

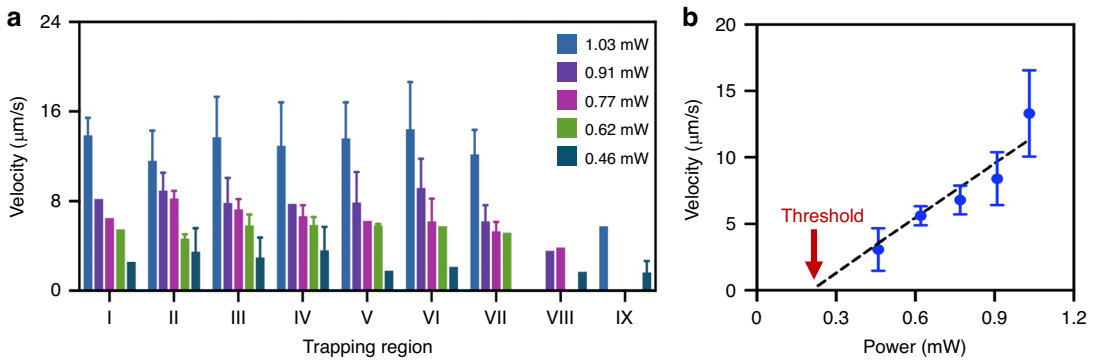

Fig. 5 Large-scale particle trapping performance of the GTP WGM microbottle resonator. a Measured velocities of particles at different optical power levels and axial trapping regions in the microbottle resonator. **b** Average velocity of trapped particles as a function of input optical power

Table 1 Comparison of different near-field optical trapping platforms

Platform	Trapping region (μm)	Particle interacting field	Localized trapping	Refs.
WGM resonator	0.5 - 3.5	Evanescent wave	No	13–16,22
Waveguide	0.35	Evanescent wave	Yes	30
Slot waveguide	0.1	Field strength antinode	No	7
Photonic crystal resonator	0.2	Field strength antinode	Yes	31
Surface plasmon polaritons	80	Evanescent wave	No	32
Photonic nanojet array	28	Field strength antinode	Yes	33
Metasurface	30	Field strength antinode	Yes	34
GTP WGM resonator	195	Field strength antinode, enhanced robustness	Yes	This work

contour of the microbottle can be expressed as

$$r_{\mathrm{inner}}(z)[\mu\mathrm{m}] = 57.55 + 49.31 \cdot e^{-6.09 \times 10^{-5} z^2} \quad (6)$$

Therefore, the wall thickness increases from the equatorial centre (1 μm) towards both axial ends (5 μm). The integrated structure was then packaged to enhance mechanical stability (see more details in Fig. S3). The experimental setup is illustrated in Fig. S4. A tunable laser (CTL 950, 920–990 nm, TOPTICA) serves as the input light source, and the polarization state is adjusted to the transverse magnetic (TM) mode via a polarization controller, thereby maximizing the light-particle interaction. The TM-mode laser light is split into two light paths with a 1:99 splitter. One path is directly connected to a power meter (S120C, Thorlabs) to obtain the reference level of the input light power. The other path is coupled to the fiber taper and evanescently coupled into the hollow optofluidic microbottle resonator, exciting the GTP WGM. Polystyrene (PS) particles (DSM01, Huge) with a radius of 500 nm were diluted into D_2O at a concentration of 10^7 particles/mL and injected into the hollow optofluidic microbottle via a syringe pump (LSP02-1B, LongerPump) using the withdrawal mode. The use of D_2O significantly reduces infrared absorption and associated heating as compared to H_2O. The velocity and viscosity of the flow are 40 μm/s and 1.2 mPa·s, respectively. To minimize particle adhesion, the microbottle's inner surface was treated with PEG-silane at 2.11 mg/mL in absolute ethanol (EtOH). The channel was then rinsed with absolute EtOH to remove unreacted silane and impurities, followed by introduction of TAE buffer to hydrate and extend the PEG chains in an aqueous environment. The optical trapping dynamics are recorded by a charge-coupled device (CCD) camera (BC4800, Bosheng) through a microscope system (BX51, Olympus), and the output WGM signal is detected by a photodetector (APD430A/M, Thorlabs).

Large-Scale Particle Trapping

The fabricated GTP WGM microbottle resonator achieves an ultra-high Q factor of approximately 2.6×10^7, as shown in Fig. S5. Using the fiber taper positioned away from the equator, high-order axial WGMs were excited to enable large-scale particle trapping. The trapping of large-scale PS particles was recorded (Supplementary Movie 1),

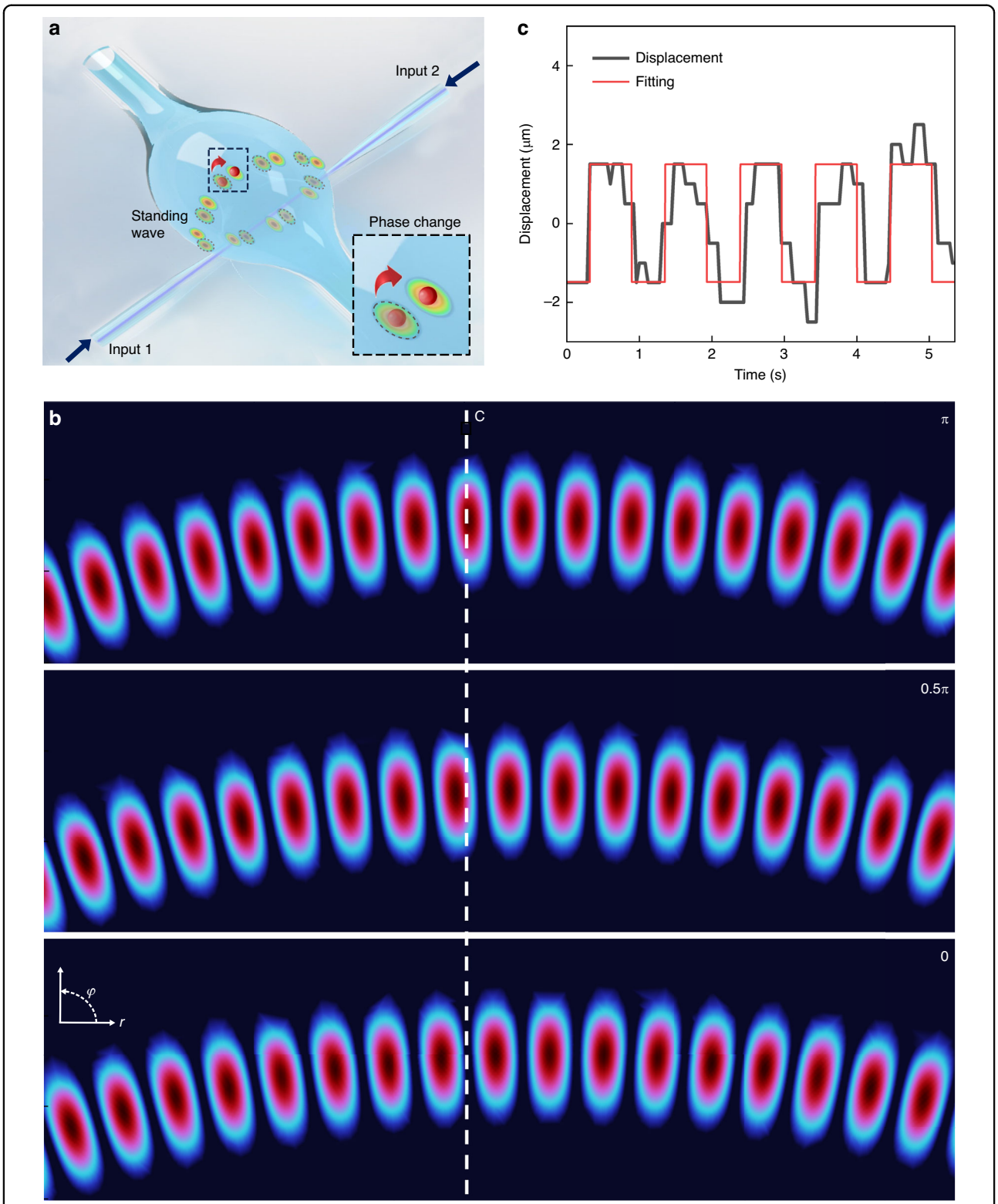

Fig. 6 Localized and tunable particle trapping via standing-wave excitation. a Schematic of counter-propagating beam coupling for standing-wave formation. **b** Standing-wave antinode displacement in equatorial plane ($r\varphi$-plane) under phase difference 0, 0.5π and π. **c** Measured azimuthal position of a trapped PS particle as the phase difference is modulated by a 1-Hz square-waveform voltage. Red curve shows a fit to a 1-Hz square-wave function

and the trapping events within a 1-min observation window are analyzed and shown in Fig. 4. 11 separate particle trapping events (labeled as **T1–T11**) are observed. Under the surface functionalization protocol, particle adhesion to the inner surface was greatly suppressed, with only occasional instances observed during experiments. A trapped particle is first subjected to axial-radial confinement, being pulled towards one of the stable axial antinodes near the inner surface of the microbottle by the strong optical gradient forces. Subsequently, the strong scattering force due to the excited GTP WGM causes an azimuthal propulsion of the trapped particle, creating a circular (orbital) trajectory along the inner surface of the microbottle at the axial antinode. In Supplementary Movie 1 with a 2D perspective of the CCD camera, such an orbital trajectory appears as a horizontal oscillating motion (left to right to left), accompanied by alternating out-of-focus and in-focus observations of the trapped particle; the non-sphericity of the particles is an imaging artifact from anisotropic lensing by the ellipsoidal, water-filled microbottle[29]. The stability of these multiple orbital motions proves that large-scale PS particles are trapped at multiple axial antinodes in the microbottle stably, even under a continuous fluid flow at 40 μm/s, due to the strong optical gradient forces in the GTP WGM resonator.

Figure 5a summarizes the velocities of trapped PS particles at various axial distances from the equatorial center under different incident optical powers. The trapping regions, Ⅰ - Ⅸ, denote areas with axial distances from the equatorial center of 0–7.5 μm, 7.5–22.5 μm, 22.5–37.5 μm, 37.5–52.5 μm, 52.5–67.5 μm, 67.5–82.5 μm, 82.5–97.5 μm, 97.5–112.5 μm, and 112.5–127.5 μm, respectively. With an input power of 1.03 mW, the microbottle resonator enables trapped particles to exhibit a uniform rotational velocity larger than 12 μm/s within an axial range extending up to ±97.5 μm (*i.e.*, 195 μm). The observed axial trapping range indicates an excited WGM axial mode order of $q \approx 278$ (see details in Supplementary Note 1 in the Supplementary Information).

Particle trapping is observed even when the input power is reduced to 0.46 mW. A series of five experiments was conducted to determine the minimum optical power for maintaining particle orbital motion. The velocities of all trapping events within the ± 97.5 μm axial range are averaged, and the results are presented in Fig. 5b. Through linear fitting, the threshold optical power for trapping 500-nm-radius PS particles is estimated to be 0.198 mW. To further evaluate the reproducibility of this performance, we fabricated and characterized two additional devices. As summarized in Fig. S6, all three devices consistently enable uniform particle rotation across the 195 μm axial span, with well-aligned velocity-power relationships, confirming satisfactory reproducibility.

As summarized in Table 1, the GTP WGM microbottle resonator offers competitive advantages over other near-field platforms. Its excitation of high-order WGMs enables large-scale (195 μm) optical trapping. This approach leverages deeply penetrating (several μm) field strength antinodes for direct and strong light-matter interaction, while the gradient wall confines the peak field within the silica to ensure exceptional robustness against perturbations. These performance benefits, together with simple fabrication and cost-effectiveness, collectively establish our device as an ideal platform for scalable optical manipulation.

Localized and Tunable Particle Trapping

Localized optical trapping is achieved at the equatorial center by exciting low-order axial WGMs, which exhibit a highly concentrated optical field suitable for forming standing waves. This is achieved by switching the laser light input to the equatorial fiber taper. To form a stable standing wave for three-dimensional particle confinement, two counter-propagating coherent beams are simultaneously coupled through this equatorial fiber taper using a 3-dB optical coupler, as illustrated in Fig. 6a. The excited counter-propagating WGMs form a standing wave at the equatorial center, where optical scattering forces from opposing directions cancel out, enabling three-dimensional particle trapping and confinement in the axial, radial, and azimuthal directions. Moreover, the standing-wave antinodes (or the particle trapping position) can be shifted along the azimuthal direction by adjusting the phase difference between the two beams. By changing the phase difference from 0 to π, the hotspot at the equatorial center will be shifted half the distance between the two hotspots along the φ direction as shown in Fig. 6b. In the experiment, we use a piezo fiber stretcher to induce phase shifts in one input beam, and the corresponding experimental setup is illustrated in Fig. S7. By applying a 1-Hz square waveform to the piezo fiber stretcher, the phase difference between the two beams is alternately changed between 0 and 12π. Figure 6c (see also Supplementary Movie 2) shows that the particle is confined but azimuthally displaced within a 3-μm region. This result demonstrates the localized particle manipulation capability of the GTP WGM microbottle resonator.

Conclusions

We theoretically and experimentally demonstrate a thin-walled hollow GTP WGM microbottle resonator for optical trapping. By exploiting the gradient-wall thickness structure, for the first time, our approach significantly enhances the anti-interference capability against trapped particles, showing a more robust particle trapping mechanism. Moreover, the GTP WGM microbottle

resonator enables large-scale particle trapping and sensing, allowing particles to rotate uniformly along multi-equatorial orbits within an extended axial range of up to 195 μm. Our experiments reveal that 500-nm-radius PS particles can be trapped with an ultralow threshold power of 0.198 mW. In addition, the GTP WGM microbottle resonator demonstrates localized and tunable optical trapping capability by using two counter-propagating coherent beams and varying their phase difference.

With its multiple particle-trapping orbits, extended trapping range and highly compact architecture, the GTP WGM microbottle resonator offers considerable potential for diverse multifunctional applications. It provides an ideal platform for high-throughput single-cell analysis, enabling parallel, real-time monitoring of the physiological dynamics of microorganisms confined within isolated orbits. The pronounced dependence of potential well depth on particle size and shape further facilitates label-free sorting of bioparticles such as yeast and *E. coli*. In addition, the rapid orbital motion of trapped particles enhances micromixing and increases surface collision frequency, thereby accelerating biochemical reactions in a manner reminiscent of catalytic processes. The platform's capacity for localized and tunable trapping also opens avenues for targeted drug loading onto carrier particles. To advance this design from laboratory proof-of-concept to practical microsystems, several challenges must be overcome, foremost among them the development of scalable, high-performance fabrication strategies. The adoption of top-down micro/nanofabrication techniques will be essential to ensure device uniformity, reproducibility, and robust performance in future implementations.

Acknowledgements
This work was financially supported by the National Natural Science Foundation of China (grant no. 62175035, X.W.), Natural Science Foundation of Shanghai (grant no. 21ZR1407400 X.W.), Hong Kong Research Grant Council/University Grants Committee (grant no. 21203724, L.K.C.) and the Hong Kong Polytechnic University (Global STEM Professorship BDA8, A.-Q.L.).

Author details
[1]College of Future Information Technology, State Key Laboratory of Photovoltaic Science and Technology, Fudan University, Shanghai, China. [2]Research Institute for Quantum Technology (RIQT), The Hong Kong Polytechnic University, Hong Kong SAR, China. [3]Department of Electrical and Electronic Engineering, The Hong Kong Polytechnic University, Hong Kong SAR, China. [4]Jiangsu Key Laboratory of Advanced Laser Materials and Devices, School of Physics and Electronic Engineering, Jiangsu Normal University, Xuzhou, China

Author contributions
Y.L. and H.W. contributed equally to this work. Y.L. and X.W. designed the research; H.W. performed the theoretical modeling and analysis. Y.L. fabricated the sensor and performed the experimental measurements. Y.L., H.W., Z.G., X.Z., Y.Z., Q.W., M.L. and H.C. analyzed the data, Y.X.L. and L.K.C. wrote the manuscript. L.K.C. and A.-Q.L. revised the manuscript. X.W. proposed the study with contributions from L.K.C. and A.-Q.L. X.W. and A.-Q.L. supervised the project.

Conflict of interest
The authors declare no competing interests.

Supplementary information The online version contains supplementary material available at https://doi.org/10.1038/s41378-026-01167-7.

Received: 16 July 2025 Revised: 5 December 2025 Accepted: 26 December 2025
Published online: 22 January 2026

References
1. Erickson, D., Serey, X., Chen, Y.-F. & Mandal, S. Nanomanipulation using near field photonics. *Lab Chip* **11**, 995–1009 (2011).
2. Chin, L. K., Shi, Y. & Liu, A.-Q. Optical forces in silicon nanophotonics and optomechanical systems: science and applications. *Adv. Dev. Instrum.* (2020).
3. Qin, J. et al. Metasurface micro/nano-optical sensors: principles and applications. *ACS Nano.* **16**, 11598–11618 (2022).
4. Shi, Y. Z. et al. Sculpting nanoparticle dynamics for single-bacteria-level screening and direct binding-efficiency measurement. *Nat. Commun.* **9**, 815 (2018).
5. Català-Castro, F. et al. Measuring age-dependent viscoelasticity of organelles, cells and organisms with time-shared optical tweezer microrheology. *Nat. Nanotechnol.* 1–10 (2025).
6. Shi, Y. et al. Trapping and detection of single viruses in an optofluidic chip. *ACS sensors* **6**, 3445–3450 (2021).
7. Yang, A. H. et al. Optical manipulation of nanoparticles and biomolecules in sub-wavelength slot waveguides. *Nature* **457**, 71–75 (2009).
8. Soltani, M. et al. Nanophotonic trapping for precise manipulation of biomolecular arrays. *Nat. Nanotechnol.* **9**, 448–452 (2014).
9. Hogan, L. T. et al. Toward real-time monitoring and control of single nanoparticle properties with a microbubble resonator spectrometer. *ACS Nano.* **13**, 12743–12757 (2019).
10. Su, L. et al. Fast single atom imaging for optical lattice arrays. *Nat. Commun.* **16**, 1017 (2025).
11. Zhou, X., Tamura, H., Chang, T.-H. & Hung, C.-L. Coupling single atoms to a nanophotonic whispering-gallery-mode resonator via optical guiding. *Phys. Rev. Lett.* **130**, 103601 (2023).
12. Vilas, N. B. et al. Magneto-optical trapping and sub-Doppler cooling of a polyatomic molecule. *Nature* **606**, 70–74 (2022).
13. Lin, S., Schonbrun, E. & Crozier, K. Optical manipulation with planar silicon microring resonators. *Nano Lett* **10**, 2408–2411 (2010).
14. Lin, S. & Crozier, K. B. Planar silicon microrings as wavelength-multiplexed optical traps for storing and sensing particles. *Lab Chip* **11**, 4047–4051 (2011).
15. Yang, A. H. & Erickson, D. Optofluidic ring resonator switch for optical particle transport. *Lab Chip* **10**, 769–774 (2010).
16. Wang, J. & Poon, A. W. Unfolding a design rule for microparticle buffering and dropping in microring-resonator-based add-drop devices. *Lab Chip* **14**, 1426–1436 (2014).
17. Wang, H., Wu, X. & Shen, D. Localized optical manipulation in optical ring resonators. *Opt. Express* **23**, 27650–27660 (2015).
18. Arnold, S. et al. Whispering gallery mode carousel–a photonic mechanism for enhanced nanoparticle detection in biosensing. *Opt. Express* **17**, 6230–6238 (2009).
19. Lopez, J. R. Snyder, K. M. Keng, D. & Arnold, S. Whispering gallery mode coulometry of the nanoparticle-microcavity interaction in aqueous solution. *Appl. Phys. Lett.* **112**, 5 (2018).
20. Ali, A. R. & Ramadan, M. W. Artificial neural networks as digital twins for whispering gallery mode optical sensors in robotics applications. *Photonic Sens.* **15**, 1–18 (2025).
21. Wang, H. & Wu, X. Optical manipulation in optofluidic microbubble resonators. *Sci. China- Phys. Mech. Astron.* **58**, 1–6 (2015).
22. Cai, H. & Poon, A. W. Optical manipulation of microparticles using whispering-gallery modes in a silicon nitride microdisk resonator. *Opt. Lett.* **36**, 4257–4259 (2011).
23. Bar-David, D., Maayani, S., Martin, L. L. & Carmon, T. Cavity optofluidics: a μdroplet's whispering-gallery mode makes a μvortex. *Opt. Express* **26**, 19115–19122 (2018).

24. Murugan, G. S., Wilkinson, J. S. & Zervas, M. N. Selective excitation of whispering gallery modes in a novel bottle microresonator. *Opt. Express* **17**, 11916–11925 (2009).
25. Humphrey, M. J., Dale, E., Rosenberger, A. T. & Bandy, D. K. Calculation of optimal fiber radius and whispering-gallery mode spectra for a fiber-coupled microsphere. *Opt. Commun.* **271**, 124–131 (2007).
26. Louyer, Y., Meschede, D. & Rauschenbeutel, A. Tunable whispering-gallery-mode resonators for cavity quantum electrodynamics. *Phys. Rev. A.* **72**, 031801 (2005).
27. Gorodetsky, M. L. & Ilchenko, V. S. Optical microsphere resonators: optimal coupling to high-Q whispering-gallery modes. *J. Opt. Soc. Am. B.* **16**, 147–154 (1999).
28. Li, Y. et al. An all-optical multidirectional mechano-sensor inspired by biologically mechano-sensitive hair sensilla. *Nat. Commun.* **15**, 2906 (2024).
29. Zhao, X. et al. Tunable optofluidic microbubble lens. *Opt. Express* **30**, 8317–29 (2022).
30. Shi, Y. et al. Optical potential-well array for high-selectivity, massive trapping and sorting at nanoscale. *Nano Lett* **20**, 5193–5200 (2020).
31. Mandal, S., Serey, X. & Erickson, D. Nanomanipulation using silicon photonic crystal resonators. *Nano Lett* **10**, 99–104 (2010).
32. Wang, K., Schonbrun, E. & Crozier, K. B. Propulsion of gold nanoparticles with surface plasmon polaritons: evidence of enhanced optical force from near-field coupling between gold particle and gold film. *Nano Lett* **9**, 2623–2629 (2009).
33. Li, Y. et al. Trapping and detection of nanoparticles and cells using a parallel photonic nanojet array. *ACS Nano* **10**, 5800–5808 (2016).
34. Conteduca, D. et al. Multiplexed near-field optical trapping exploiting anapole states. *ACS Nano* **17**, 16695–16702 (2023).